Article

Quantification of Precipitation Using Polarimetric Radar Measurements during Several Typhoon Events in Southern China

Qiulei Xia [1], Wenjuan Zhang [2], Haonan Chen [3,4], Wen-Chau Lee [5], Lei Han [6,*], Yu Ma [7] and Xiantong Liu [8]

[1]   College of Electronic Engineering, Chengdu University of Information Technology, Chengdu 610225, China; 3170302009@cuit.edu.cn
[2]   State Key Laboratory of Severe Weather, Chinese Academy of Meteorological Sciences, Beijing 100081, China; zwj@cma.gov.cn
[3]   NOAA Physical Sciences Laboratory, Boulder, CO 80305, USA; haonan.chen@noaa.gov
[4]   Cooperative Institute for Research in the Atmosphere, Fort Collins, CO 80523, USA
[5]   National Center for Atmospheric Research, Boulder, CO 80301, USA; wenchau@ucar.edu
[6]   College of Information Science and Engineering, Ocean University of China, Qingdao 266100, China
[7]   Department of Hydraulic Engineering, State Key Laboratory of Hydroscience and Engineering, Tsinghua University, Beijing 100084, China; mayu15@mails.tsinghua.edu.cn
[8]   Institute of Tropical and Marine Meteorology, China Meteorological Administration, Guangzhou 510080, China; xtliu@gd121.cn
*   Correspondence: hanlei@ouc.edu.cn; Tel.: +86-532-6678-2368

check for updates

Abstract: Accurate quantitative precipitation estimation (QPE) during typhoon events is critical for flood warning and emergency management. Dual-polarization radar has proven to have better performance for QPE, compared to traditional single-polarization radar. However, polarimetric radar applications have not been extensively investigated in China, especially during extreme events such as typhoons, since the operational dual-polarization system upgrade only happened recently. This paper extends a polarimetric radar rainfall system for local applications during typhoons in southern China and conducts comprehensive studies about QPE and precipitation microphysics. Observations from S-band dual-polarization radar in Guangdong Province during three typhoon events in 2017 are examined to demonstrate the enhanced radar rainfall performance. The microphysical properties of hydrometeors during typhoon events are analyzed through raindrop size distribution (DSD) data and polarimetric radar measurements. The stratiform precipitation in typhoons presents lower mean raindrop diameter and lower raindrop concentration than that of the convection precipitation. The rainfall estimates from the adapted radar rainfall algorithm agree well with rainfall measurements from rain gauges. Using the rain gauge data as references, the maximum normalized mean bias (*NMB*) of the adapted radar rainfall algorithm is 20.27%; the normalized standard error (*NSE*) is less than 40%; and the Pearson's correlation coefficient (*CC*) is higher than 0.92. For the three typhoon events combined, the *NSE* and *NMB* are 36.66% and -15.78%, respectively. Compared with several conventional radar rainfall algorithms, the adapted algorithm based on local rainfall microphysics has the best performance in southern China.

Keywords: dual-polarization radar; quantitative precipitation estimation; typhoon; Southern China

1. Introduction

Tropical cyclones are extreme weather phenomena often accompanied by high winds and heavy rainfall, which may result in significant socioeconomic losses in coastal areas. Therefore, numerous

studies have focused on radar-based quantitative precipitation estimation (QPE) and forecast (QPF) during Atlantic hurricanes, and Australian and Indian cyclones [1,2]. However, polarimetric radar QPE applications for typhoon events in China are relatively rare, partly because the operational weather radar network has just been upgraded with dual-polarization capabilities. In addition, there is a lack of comprehensive analysis of QPE and associated precipitation microphysics during typhoon events.

Compared to traditional single-polarization radar, the dual-polarization radar can provide polarimetric measurements, including differential reflectivity Z_{DR}, differential phase Ψ_{DP}, co-polar correlation coefficient ρ_{HV}, and the specific differential phase shift K_{DP} [3,4]. These polarimetric observations directly reflect the microphysical properties of hydrometeors, including precipitation particle shape and size distributions [5], and thus can be used to estimate the precipitation rate and amount [6–13]. In fact, dual-polarization radar has become an essential tool to study severe weather and mitigate the resultant natural disasters. In this paper, using S-band polarimetric measurements during three typhoon events, we develop an adapted rainfall system that includes data quality control (QC), data segmentation, hydrometeor classification, and precipitation quantification. The QC method used in this paper can effectively identify and mitigate the ground clutter and environmental noises, through differential phase and clutter processing. The data segmentation method is applied to reduce the impact of blockage and beam broadening. Depending on the distance of the target from the radar, data from different elevation angles are selected for QPE. The hydrometeor classification algorithm (HCA) [14], based on traditional fuzzy-logic approach and *K*-means clustering, is used to obtain classification results with the polarimetric parameters (Z_H, Z_{DR}, ρ_{HV}, K_{DP}) and environment temperature information T observed from a local sounding station. The classification results and polarimetric parameters determine the selection of rainfall relations, which are acquired through simulation based on local raindrop size distribution (DSD) data.
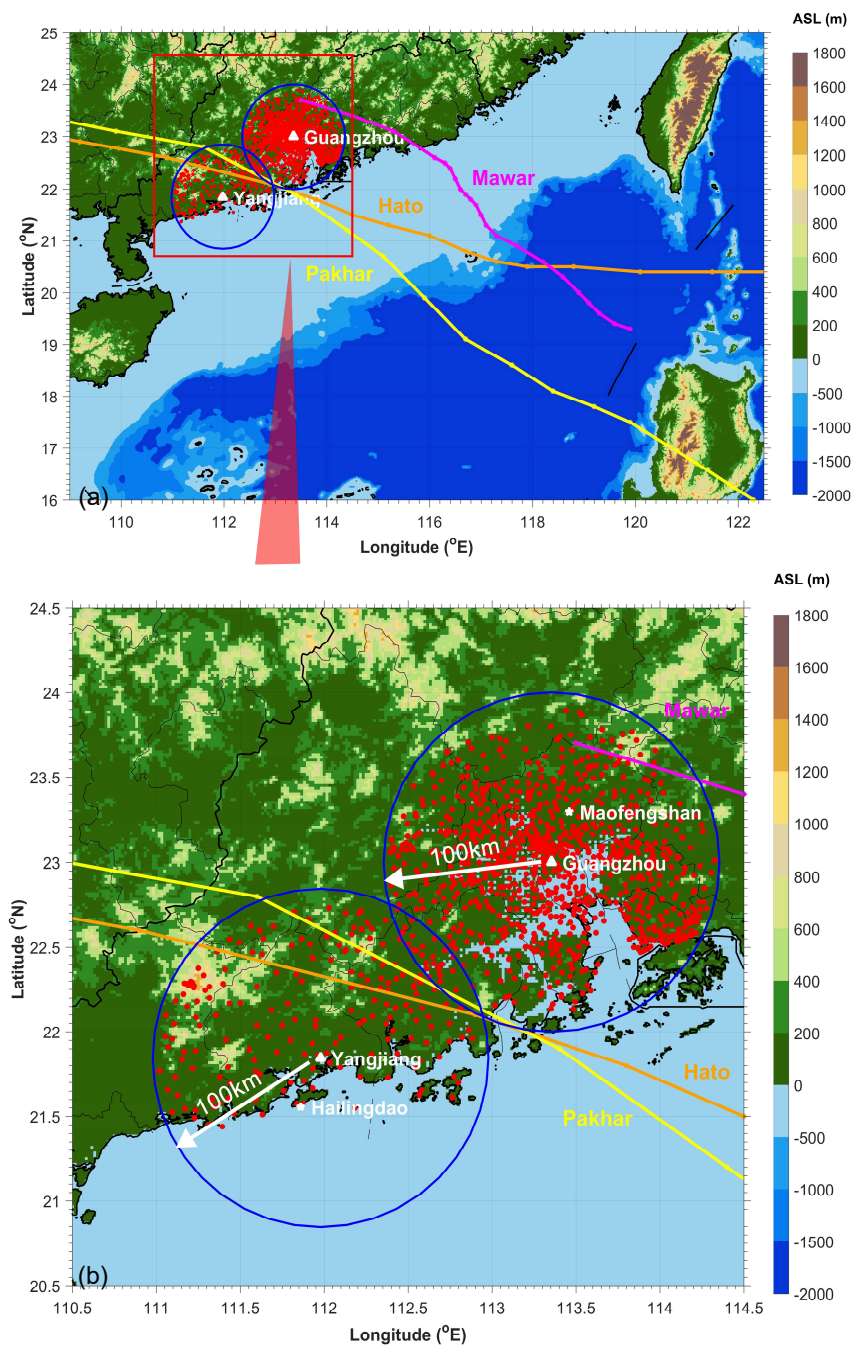
Observations from the upgraded S-band dual-polarization radars are used to demonstrate the QPE performance of the adapted algorithm, and the polarimetric observations can also indicate typhoon features such as typhoon eye, strong convective area and precipitation particle size distributions. Using DSD data and S-band polarimetric measurements during the three typhoon events, this paper also examines the microphysical properties of typhoon-induced precipitation. Overall, we hope to promote polarimetric radar applications during typhoon events in China, through this comprehensive study which combines QPE and precipitation microphysical properties observed by in situ instruments.

The rest of this paper is organized as follows. Section 2 describes the study domain, datasets, and the adapted polarimetric radar rainfall algorithm. The typhoon events, radar observations, and the microphysical properties of typhoon-induced precipitation are presented in Section 3. Section 4 provides the QPE results and quantitative evaluation based on surface rain gauge measurements. The main findings of this study and suggested future work are summarized in Section 5.

2. Datasets and Methodology

2.1. Study Domain

The study domain of this research is located in Guangdong Province in southern China, which has the largest number of typhoon landfalls in China, with an average of 2 to 3 each year [15]. The whole territory of Guangdong is between 20°13′–25°31′N and 109°39′–117°19′E, with high mountains in the north and west, and plains and low hills in the south (Figure 1). Climatologically, Guangdong is located in the East Asian monsoon region, with an average annual precipitation of 1300–2500 mm. Affected by monsoon and terrain, the annual precipitation in the southern region is generally higher than the northern part. Figure 1 shows the study domain and locations of the observational instruments used in this study, overlaid with the best tracks and landing locations of the three typhoons included in this study.

Figure 1. (**a**) The best tracks of Typhoons Hato (orange line), Pakhar (yellow line), and Mawar (magenta line); (**b**) Locations of rain gauges (red asterisks), S-band dual-polarization radars (white triangles) and disdrometers (white pentagram) in Guangzhou and Yangjiang overlaid on the terrain. The two blue circles denote the 100 km coverage range of the radar.

2.2. Radar and Rain Gauge Data

According to the strategic plan of the China Meteorological Administration, 140 dual-polarized radars will be deployed nationwide by the end of 2020. The upgraded China New Generation of Weather Radars (CINRADs) are expected to improve the forecasting and warning capabilities against severe weather such as heavy rainfall, hail, and typhoons. Eight weather radars in Guangdong completed the dual-polarization upgrade in 2016; this is the first batch of the dual-polarization upgrade. This study uses data from two of them, i.e., Guangzhou and Yangjiang stations. The Yangjiang radar is closer to the best tracks of Typhoons Hato and Pakhar, whereas the Guangzhou radar is closer to the
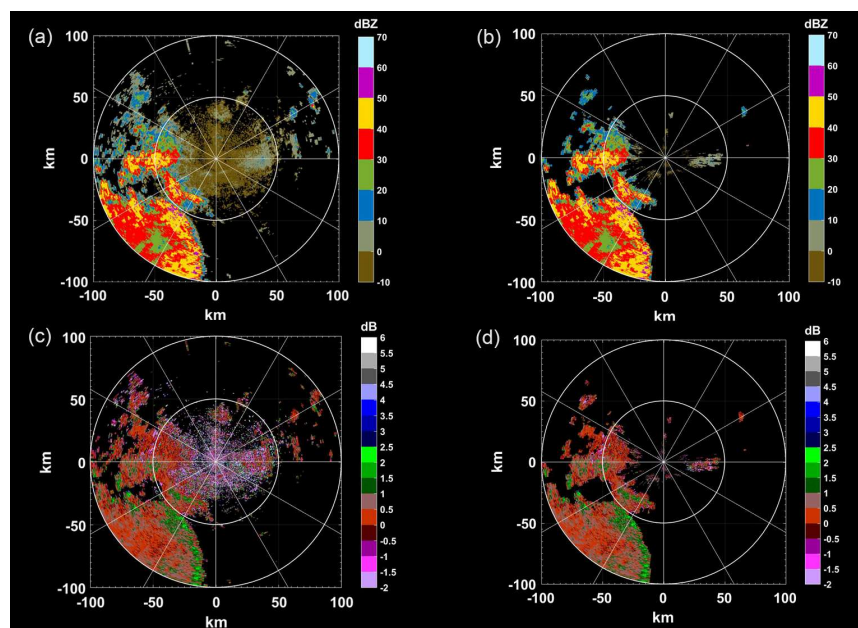
best track of Typhoon Mawar. Therefore, the data from the Yangjiang radar during Typhoons Hato and Pakhar are used, and the data from the Guangzhou radar during Typhoon Mawar are used. As shown in Figure 1, the Yangjiang radar (21.845°N, 111.979°E) is deployed in Jishan, and the Guangzhou radar (23.004°N, 113.355°E) is deployed in Dazhengang. The two radars are deployed on the mountains, mainly to avoid beam blockages due to high-rise buildings. The model of the radars is CINRAD/SA (S stands for S-band, A refers to the manufacturer of Beijing Metstar Radar Company). The scan strategy is volume coverage pattern (VCP) 21, which includes nine elevation angles, i.e., 0.5°, 1.5°, 2.4°, 3.3°, 4.3°, 6°, 9.9°, 14.6°, and 19.5°. The volume scan update cycle is six minutes. The detailed system specifications of CINRAD/SA are shown in Table 1.

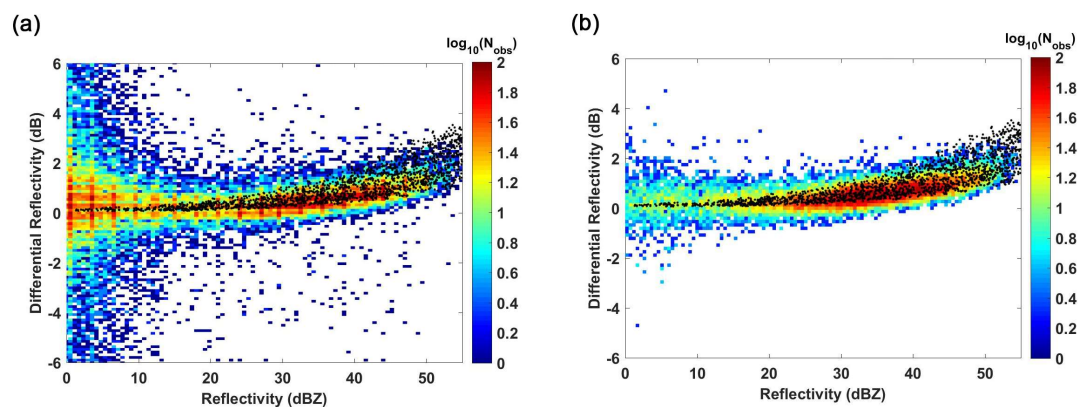**Table 1.** System specifications of the radars at Guangzhou and Yangjiang in Guangdong Province.

Type	Radar Name	
	Yangjiang Radar	**Guangzhou Radar**
Antenna altitude (m)	106	179
Frequency (MHZ)	2783	2885
Polarization	Dual linear	Dual linear
Pulse width (ns)	1570	1570
Peak power output (kW)	650	650
Cut number	11	11
Range gates	1840	1840
Sampling resolution (m)	250	250
Beam width (degree)	0.92	0.92

Radar data quality control is indispensable before quantitative applications. The building occlusion, ground clutters, and environmental noises can all affect the accuracy of the application products. In this paper, a compound QC method based on differential phase and clutter processing is used to identify and mitigate the non-meteorological echoes, including ground clutters [16–19]. Differential phase processing is mainly performed to smooth the differential phase, which includes phase unfolding, clutter suppression, range filtering, and least square fitting. Sample observations from the Yangjiang radar 1.5-degree which sweep at 2112 UTC, 23 August 2017, before and after data QC, are shown in Figure 2. It can be seen that most of the ground clutter is suppressed after QC. Figure 3 shows the scatter density plots of Z_{DR} versus Z_H before and after data QC for a single plan position indicator (PPI) scan at 2112 UTC, 23 August 2017. The black dots overlaid with the color plots are the simulated radar moments. This study evaluates the data QC performance through comparison with the simulated radar moments, including Z_H and Z_{DR}. The radar moments are simulated using the *T*-matrix method [20]. Therein, the raindrop shape model is assumed to follow the one described by Thurai et al. [21]. The temperature used in the simulation is 20 °C, which is obtained from nearby sounding data. The overlapping ratios of Z_{DR} versus Z_H are investigated, to qualitatively demonstrate the QC performance. Apparently, the data after QC are clearer and agree better with the simulated radar moments, demonstrating the effectiveness of the implemented QC method.

Figure 2. Sample observations from the Yangjiang radar 1.5-degree sweep at 2112 UTC, 23 August 2017: (**a**) measured Z_H; (**b**) Z_H after data quality control; (**c**) measured Z_{DR}; (**d**) Z_{DR} after data quality control.
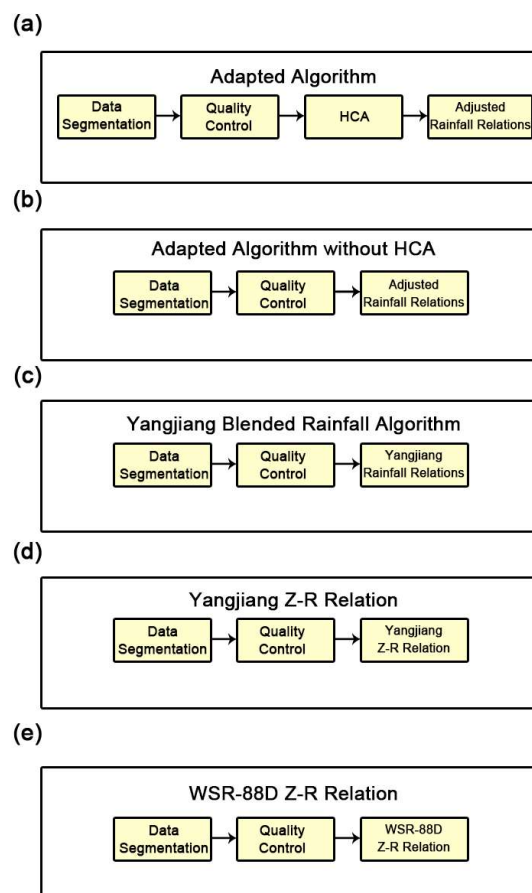

Figure 3. (**a**) Z_{DR} versus Z_H before data quality control; (**b**) Z_{DR} versus Z_H after data quality control. The black dots are the simulated radar moments based on raindrop size distribution data.

In addition, a data segmentation method is applied to further decrease the impact of blockage and ground clutter. For example, since the 0.5-degree beam from the Yangjiang radar is blocked by the terrain [22,23], this study uses a higher elevation scan to produce complete QPE. However, while the selection of higher elevation angle data could decrease the impact of blockage, it may increase the difference between radar estimates and ground gauges, due to the height differences. This issue is further compounded by the beam broadening of S-band radar at long ranges. In the segmentation, data from different elevation angles are selected for precipitation estimation, depending on the distance of the target from the radar. In particular, the elevation angles of 2.4 degrees, 1.5 degrees, and 0.5 degrees are selected within the ranges of 20–35 km, 35–60 km, and 60–100 km, respectively, from the radar.
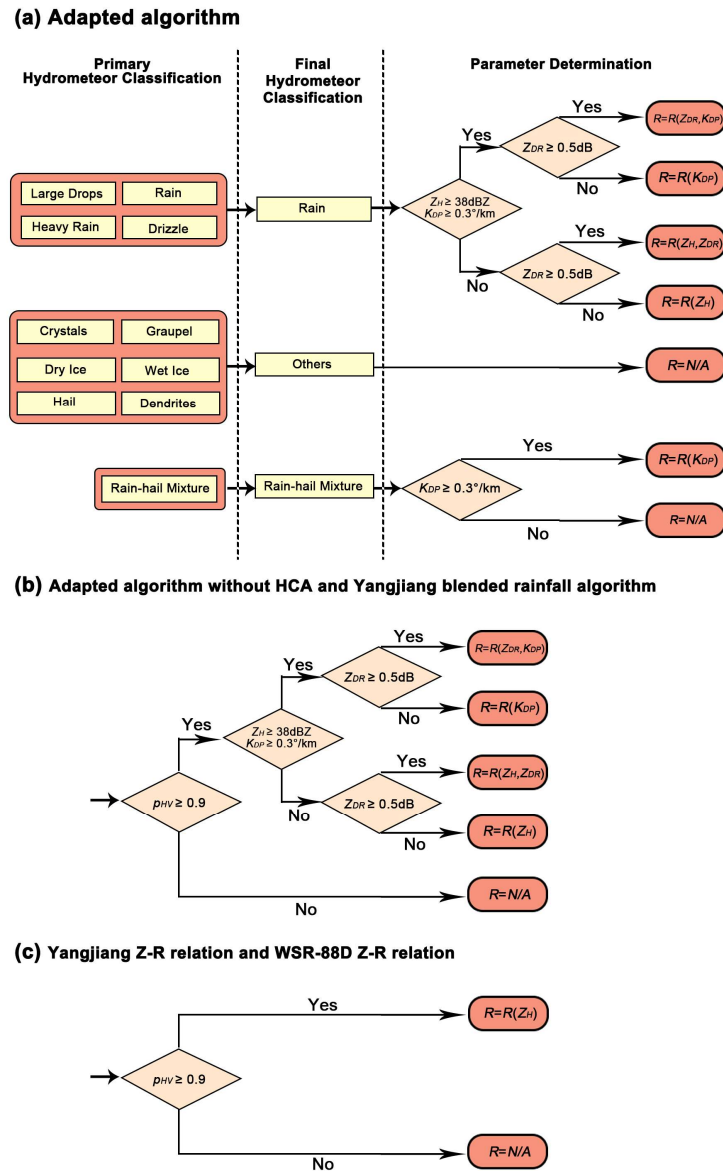
The rainfall estimates based on the dual-polarization radars are compared with rain gauge measurements, to demonstrate the performance of radar QPE. The location of the rain gauges is shown in Figure 1. There are 198 and 809 rain gauges within 100 km of the Yangjiang and Guangzhou radars, respectively. These rain gauges record rainfall rate at hourly scales.

2.3. Adapted Algorithm

This study uses five radar QPE algorithms (Figure 4), including the adapted algorithm, to estimate rainfall during these typhoon events and cross compare the performance of different algorithms. All algorithms are implemented after the data QC and segmentation processing. The HCA, only included in the adapted algorithm, is essentially based on the methodology detailed in Bechini and Chandrasekar [14]. Figure 5a shows the flowchart of the HCA-driven adapted rainfall algorithm, which selects different rainfall relations, based on the hydrometeor classification results and polarimetric parameters. Other algorithms (Figure 5b,c) without HCA compute rainfall rate through incorporating the co-polar correlation coefficient ρ_{HV}.

Figure 4. Differences between the various radar rainfall algorithms applied in this paper: (**a**) adapted algorithm; (**b**) adapted algorithm without hydrometeor classification algorithm (HCA); (**c**) Yangjiang blended rainfall algorithm; (**d**) Yangjiang Z–R relation; (**e**) WSR-88D Z–R relation. Compared to the Yangjiang blended rainfall algorithm, the adapted algorithm has different specific rainfall relations and HCA. The adapted algorithm without HCA has the same modules as the adapted algorithm except HCA. The Yangjiang blended rainfall algorithm has more rainfall relations rather than the Yangjiang Z–R relation.

(a) Adapted algorithm

(b) Adapted algorithm without HCA and Yangjiang blended rainfall algorithm

(c) Yangjiang Z-R relation and WSR-88D Z-R relation

Figure 5. The flowcharts of the rainfall algorithms: (**a**) adapted rainfall algorithm selects different specific rainfall relations based on the hydrometeor classification results, as well as the polarimetric parameters (adapted from Figure 2 in Chen et al. [17]); (**b**) adapted rainfall algorithm without HCA and Yangjiang blended rainfall algorithm; (**c**) Yangjiang Z–R relation and WSR-88D Z–R relation.

The specific rainfall relations of the adapted algorithm with and without HCA are as follows:

$$R(Z_H) \ = \ 0.02 \times 10^{0.07729Z_H} \tag{1a}$$

$$R(K_{DP}) \ = \ 51.64K_{DP}^{0.7226} \tag{1b}$$

$$R(Z_H, Z_{DR}) \ = \ 0.01172 \times 10^{0.0925Z_H}10^{-0.4035Z_{DR}} \tag{1c}$$

$$R(Z_{DR}, K_{DP}) \ = \ 75.08K_{DP}^{0.9191}10^{-0.1861Z_{DR}} \tag{1d}$$

where Z_H (dBZ) is the horizontal reflectivity factor and Z_{DR} (dB) is the differential reflectivity. The DSD data collected by a disdrometer in Yangjiang, Guangdong, during April to July 2014, are used to obtain these specific rainfall relations through nonlinear regression. The estimates are computed with these specific rainfall relations, and then the rainfall relation coefficients are adjusted, with an overall bias

ratio computed from radar estimates and corresponding rain gauge measurements. The Yangjiang blended rainfall relations are as follows:

$$R(Z_H) = 0.0093 \times 10^{0.07386Z_H} \tag{2a}$$

$$R(K_{DP}) = 31.2195K_{DP}^{0.9143} \tag{2b}$$

$$R(Z_H, Z_{DR}) = 0.024 \times 10^{0.08242Z_H}10^{-0.4913Z_{DR}} \tag{2c}$$

$$R(Z_{DR}, K_{DP}) = 59.2626K_{DP}^{0.9573}10^{-0.1317Z_{DR}} \tag{2d}$$

The rainfall relations of the blended Yangjiang algorithm are derived based on the same DSD data, but these rainfall relations are not adjusted. The Yangjiang Z–R relation only contains $R(Z_H)$ (Equation (2a)), and the WSR-88D Z–R relation is as follows:

$$R(Z_H) = 0.017 \times 10^{0.0714Z_H} \tag{3}$$

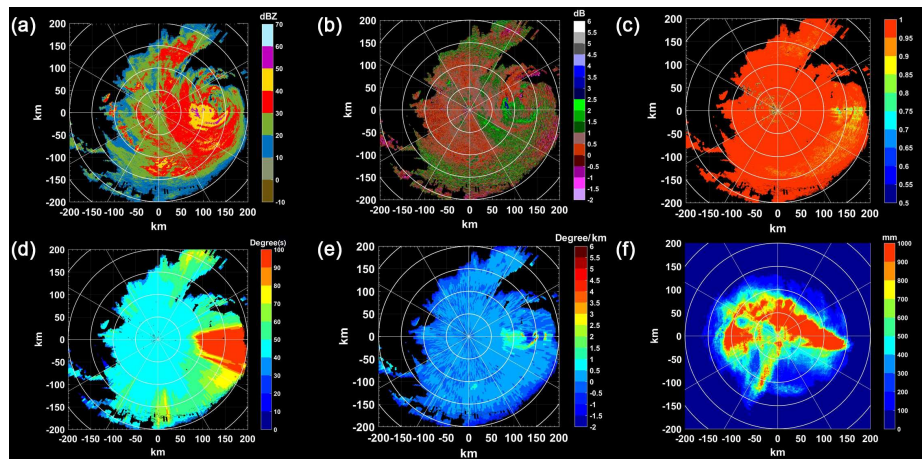This relation is generally applied for convective rain [24].

The Yangjiang and Guangzhou radars collect volume observations every six minutes, whereas the rain gauges record the rainfall rate at hourly time intervals. Therefore, the rainfall estimates computed by various algorithms need to be interpolated to match the rain gauge measurements. The radar rainfall rates are calculated using piecewise cubic Hermite interpolating polynomial (PCHIP) into 1-min resolution and then used to compute the hourly rainfall rate to compare with corresponding rain gauge measurements.

3. Description of the Typhoon Events

3.1. Super Typhoon Hato (2017)

Super Typhoon Hato formed in the northwest Pacific, 1200 km southeast of Shantou (20.4°N, 128.0°E) at 1800 UTC, 19 August 2017. While it moved northwest toward Guangdong Province, it reached severe tropical storm strength, with a maximum wind speed of 25 m s^{-1} at 0000 UTC 22 August. It then landed in Zhuhai, Guangdong Province at 0450 UTC on 23 August with severe typhoon strength (the maximum wind speed of 45 m s^{-1}). It continued to move westward through Jiangmen, Yangjiang, Maoming, and Yunfu after the landfall. Hato weakened into a tropical storm, with a maximum wind speed of 18 m s^{-1} at 0000 UTC on 24 August, and further depressed into a low pressure at 0600 UTC on 24 August. Hato was the strongest typhoon that caused landfall in China in 2017. Its landfall brought widespread heavy rainfall to western Guangdong. According to the China National Meteorological Center (NMC), a total of 17 rain gauges recorded a cumulative rainfall of more than 250 mm and 243 rain gauges recorded a cumulative rainfall of 100–250 mm from 0000 UTC 23 August to 0800 UTC 24 August 2017.

Figure 6 shows sample observations of Z_H, Z_{DR}, ρ_{HV}, Ψ_{DP}, and K_{DP} from the Yangjiang radar at 0430 UTC on 23 August. A rainfall accumulation map is also shown for illustration purposes, which is computed by the adapted algorithm based on 1.5-degree scans from 0000 UTC to 2300 UTC, 23 August 2017. It can be clearly seen that the center of the typhoon is 150 km east of the radar, and there is a strong convective area with reflectivity (Z_H) of over 40 dBZ south of the typhoon center (Figure 6a). The ρ_{HV} value of this area is less than 0.95, indicating the occurrence of rain and hail near the center of typhoon (Figure 6c). The Ψ_{DP} and K_{DP} near the center of the typhoon are obviously greater than the other regions (Figure 6d,e).

Figure 6. Sample observations from the Yangjiang radar 1.5-degree sweep at 0430 UTC, 23 August 2017: (**a**) Z_H; (**b**) Z_{DR}; (**c**) ρ_{HV}; (**d**) Ψ_{DP}; and (**e**) K_{DP}. (**f**) The rainfall accumulation computed by the adapted algorithm from 0000 UTC to 2300 UTC, 23 August 2017.

In addition, the rainfall accumulation computed by the adapted algorithm in most of the region within a range of 200 km of the radar exceeds 900 mm (Figure 6f). The time-series comparison of radar moments computed by DSD data with *T*-matrix method and measured polarimetric parameters are shown in Figure 7. It shows that precipitation in the position of the disdrometer mainly occurred from 0000 UTC to 1100 UTC and 2100 UTC to 2300 UTC 23 August 2017. The measured Z_H, Z_{DR} and K_{DP} are close to the values of simulated radar moments during this typhoon event, which indicates the reliability of the radar data.
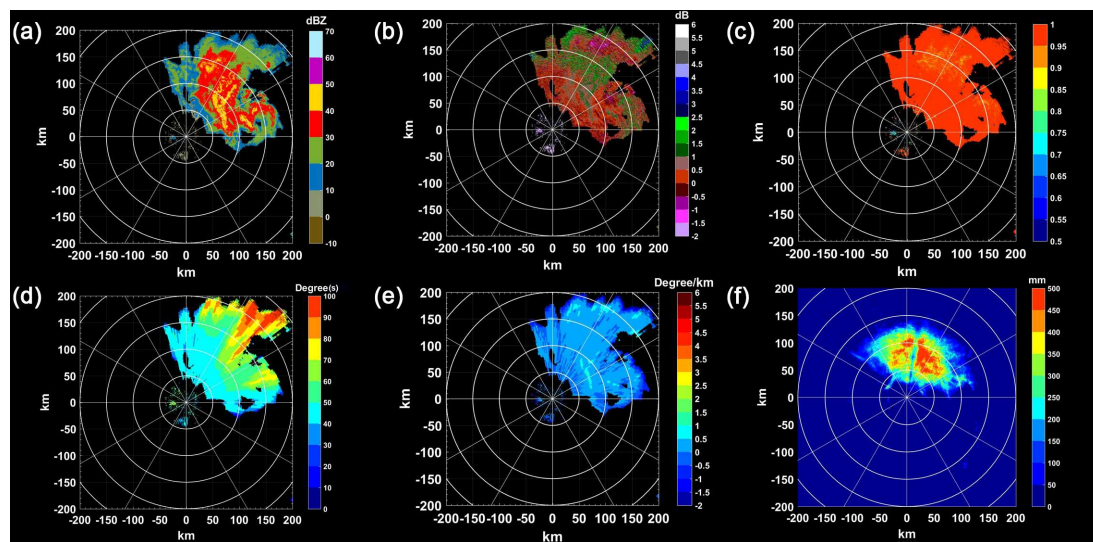

Figure 7. The time-series comparison of radar moments simulated by raindrop size distribution (DSD) data with T-matrix method and measured polarimetric parameters during Super Typhoon Hato: (**a**) Z_H, (**b**) Z_{DR}, (**c**) K_{DP}.

3.2. Severe Tropical Storm Pakhar (2017)

Severe tropical storm Pakhar formed at 0600 UTC on 24 August 2017 in the northwestern Pacific, 310 km to the north–east of Manila (15.4°N, 123.8°E), with a central pressure of 995 hPa. After crossing the Philippines and entering the South China Sea, it further intensified into a severe tropical storm and continued to move northwestward. Pakhar caused landfall in Taishan, Guangdong Province at 0100 UTC on 27 August, with a maximum wind speed of 33 m s^{-1}. After the landfall, it moved northwestward and passed through Jiangmen, Yangjiang, and Yunfu. Pakhar further weakened into a tropical depression in Guigang at 1200 UTC on 27 August. According to the NMC, from 1200 UTC 26 to 0000 UTC 29 August, the 24-hour average precipitation of Guangdong Province was 72.1 mm. A total of 44 rain gauges recorded a cumulative rainfall of > 250 mm, and 642 rain gauges recorded a cumulative rainfall of 100–250 mm. Figure 8 shows the sample observations of Z_H, Z_{DR}, ρ_{HV}, Ψ_{DP},
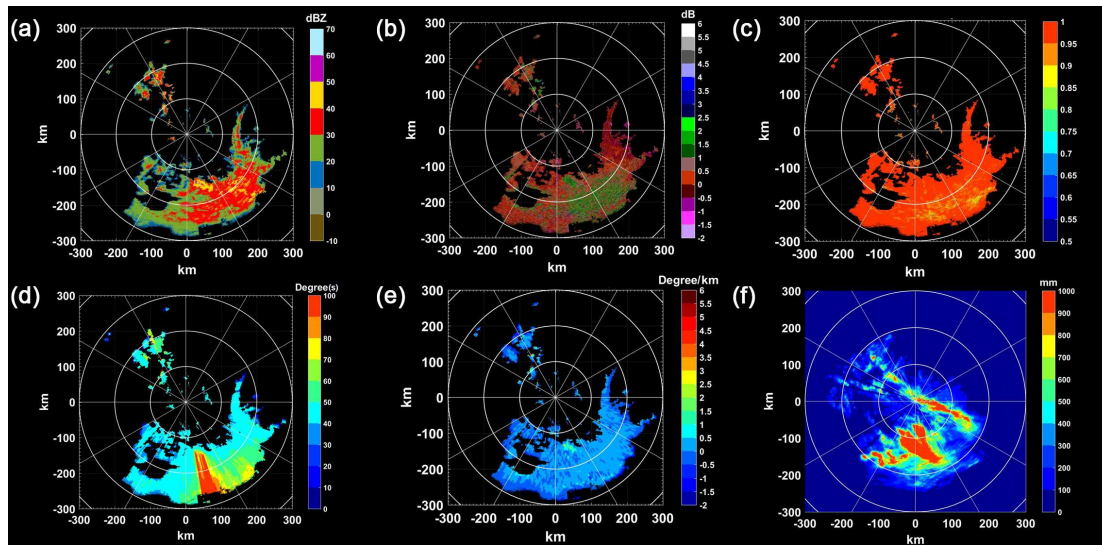
and K_{DP} from the Yangjiang radar 1.5-degree sweep at 0012 UTC on 27 August. Similarly, the rainfall accumulation from 0000 UTC to 1200 UTC, 27 August 2017, is illustrated, which is based on the adapted algorithm. The typhoon center is 150 km east of the radar, and the value of Z_H exceeds 40 dBZ. The value of Z_{DR} at 75 km northeast of the radar exceeds 2 dB and the value of the co-polar correlation coefficient exceeds 0.95 (Figure 8), indicating the large size of raindrops in this area. The region of heavy precipitation is located in the north of the Yangjiang radar. However, there was no rain at the disdrometer during this typhoon event.
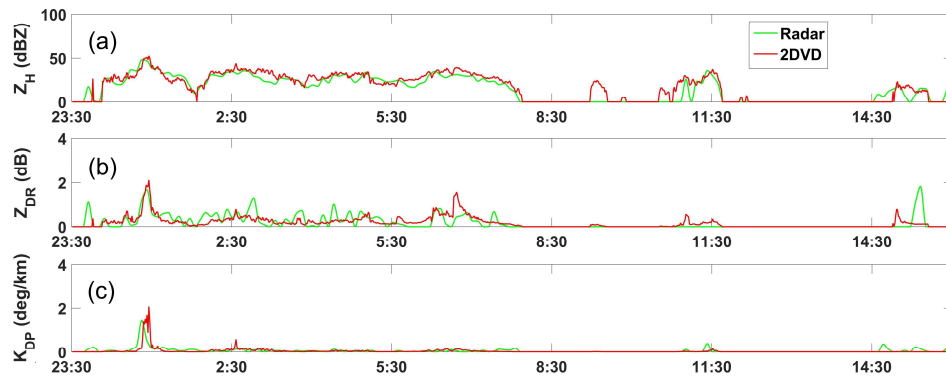

Figure 8. Same as Figure 6, but at 0012 UTC, 27 August 2017. The rainfall accumulation is from 0000 UTC to 1200 UTC, 27 August 2017.

3.3. Severe Tropical Storm Mawar (2017)

Severe tropical storm Mawar developed as a tropical depression about 690 km to the south–east of Shenzhen (18.7°N, 119.3°E) at 0000 UTC, 31 August 2017, in the northwest Pacific. First taking a northwestward course over the north of the South China Sea, Mawar became a tropical storm, with a maximum wind speed of 25 m s^{-1}. It then landed in Shanwei, Guangdong Province at 1330 UTC on 3 September, as a tropical storm with a maximum wind speed of 23 m s^{-1}. After the landfall, it weakened into a low pressure at 0200 UTC on 4 September. Mawar was the third typhoon that caused landfall in Guangdong Province in the two weeks during late August 2017. According to the NMC, from 0000 UTC on 3 September to 0000 UTC on 5 September, the 24-hour average precipitation of Guangdong Province was 39.9 mm, with the largest rainfall occurring in the Pearl River Delta. Figure 9 shows the sample observations of Z_H, Z_{DR}, ρ_{HV}, Ψ_{DP}, and K_{DP} from the Guangzhou radar 0.5-degree sweep at 1542 UTC, 3 September 2017. The rainfall accumulation is computed by the adapted algorithm from 1600 UTC on 3 September to 1600 UTC on 4 September, and it is based on 0.5-degree scans. Moreover, Figure 10 shows the time-series comparison of radar moments simulated by DSD data with the *T*-matrix method, and measured polarimetric parameters. It shows that precipitation in the position of the disdrometer mainly occurred from 2330 UTC on 3 September to 1600 UTC on 4 September, and the measured Z_H, Z_{DR} and K_{DP} are close to the values of simulated radar moments during this typhoon event.

Figure 9. Sample observations from the Guangzhou radar 0.5-degree sweep at 1542 UTC, 3 September 2017: (**a**) Z_H; (**b**) Z_{DR}; (**c**) ρ_{HV}; (**d**) Ψ_{DP}; and (**e**) K_{DP}. (**f**) The rainfall accumulation computed by the adapted algorithm from 1600 UTC on 3 September to 1600 UTC on 4 September 2017.

Figure 10. The time-series comparison of radar moments simulated by DSD data with T-matrix method and polarimetric parameters during Severe Tropical Storm Mawar: (**a**) Z_H, (**b**) Z_{DR}, (**c**) K_{DP}.

3.4. Microphysical Properties of Typhoon-induced Precipitation

In this section, the microphysical properties of typhoon-induced rainfall are investigated. The mass-weighted mean diameter D_M and the intercept parameter N_W, which can reflect the DSD characteristics [25], are calculated from the DSD data:
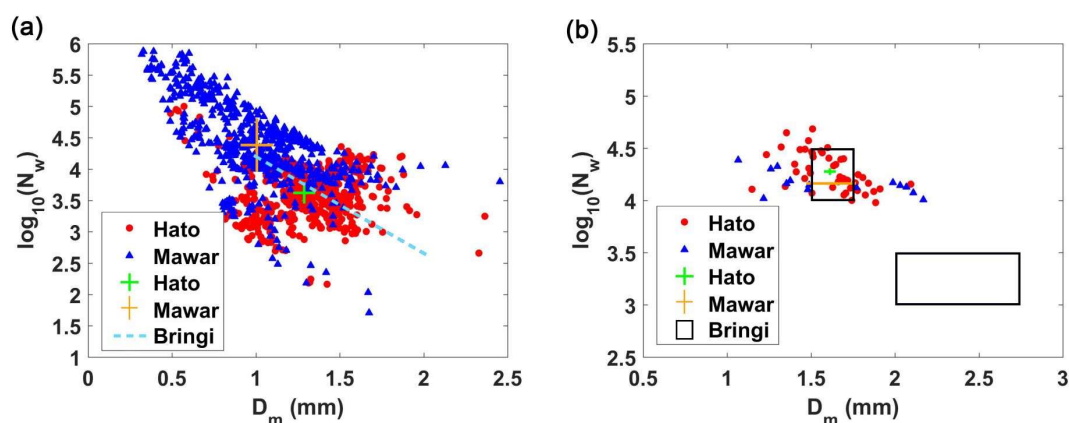
$$D_M = \frac{\int N(D)D^4 dD}{\int N(D)D^3 dD}, \tag{4a}$$

$$N_W = \frac{4^4}{\pi \rho_W}\left(\frac{W}{D_M^4}\right), \tag{4b}$$
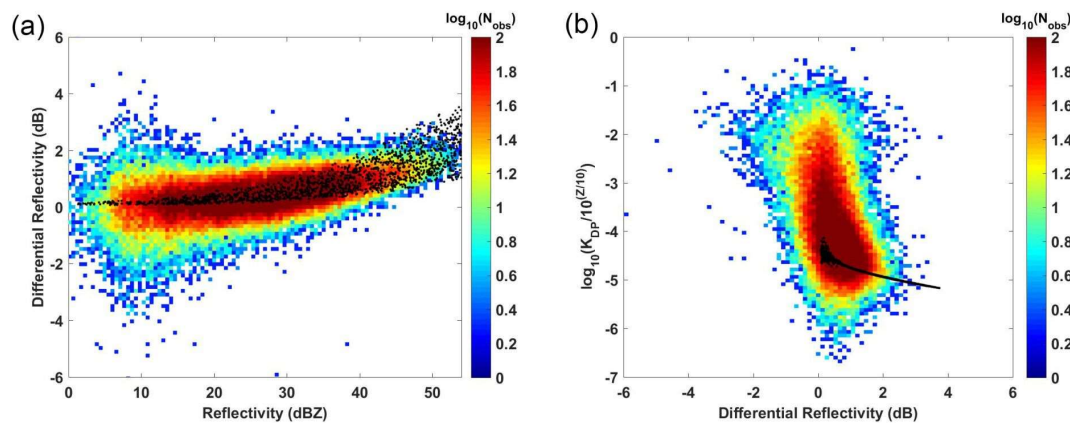
$$W = \frac{\pi}{6}\rho_W \int N(D)D^3 dD, \tag{4c}$$

where D (mm) stands for equivalent diameter; $N(D)$ (mm$^{-1}\cdot$m^{-3}) is the number concentration of raindrop per unit volume per unit size interval; ρ_W is the water density; W is the water content. Figure 11 shows the D_M versus $\log_{10} N_W$ of the stratiform (reflectivity Z_H at the height of 3 km is less than 40 dBZ) and convective system (reflectivity Z_H at the height of 3 km is larger than 40 dBZ),

which were retrieved from DSD data during typhoons Hato and Mawar. The intersection of the cross indicates average values of D_M and $\log_{10} N_W$, and the lengths of the horizontal line and the vertical line indicate variances of D_M and $\log_{10} N_W$, respectively. Figure 11 also shows the D_M and $\log_{10} N_W$ for the convective system (including maritime and continental type) and the stratiform system from Bringi et al. 2003 [25]. The maritime (continental) type of convective system presents $D_M \sim$1.5–1.75 mm (2–2.75 mm) and $\log_{10} N_W \sim$4–4.5 (3–3.5), and the stratiform precipitation system has $D_M \sim$1.25–1.75 mm and $\log_{10} N_W \sim$3–4. The raindrop characteristics for the convective system during Typhoon Hato in this study are consistent with that in maritime convective precipitation from Bringi et al. 2003 [25], while the raindrop characteristics of stratiform precipitation during Typhoon Hato are smaller (Figure 11a). For Typhoon Mawar, convective and stratiform precipitation demonstrate smaller sizes and higher concentrations of raindrops than those in Typhoon Hato (Figure 11). Differences in microphysical processes may lead to different raindrop distributions in individual typhoons. An investigation on the raindrop characteristics of typhoons landing in China shows that convective precipitation in typhoons presents a lower raindrop diameter and a higher raindrop concentration than that of the maritime convection [26]. Our results for Typhoon Mawar are in accordance with this conclusion.

Figure 11. D_M versus $\log_{10} N_W$ for (**a**) stratiform and (**b**) convective rain during Typhoons Hato (red dot) and Mawar (blue triangle). The green and orange crosses indicate means (cross centers) and standard deviations of D_M and $\log_{10} N_W$ for Typhoons Hato and Mawar, respectively. The light blue dashed line in (**a**) represents stratiform rainfall in Bringi et al. [25] The black rectangles in (**b**) represent the maritime (the left one) and continental (the right one) types of convective rainfall.

The radars observed the polarimetric parameters, including Z_H, Z_{DR} and K_{DP}, from 0000 UTC to 2300 UTC, 23 August, 0000 UTC to 1200 UTC, 27 August, and 1600 UTC, 3 September to 1600 UTC, 4 September. These polarimetric observations can reflect the microphysical properties of hydrometeors, including precipitation particle shape and size distributions. Figure 12 shows the scatter density plots of Z_{DR} versus Z_H and $\log_{10}\left[K_{DP}/\left(10^{Z_H/10}\right)\right]$ versus Z_{DR} for three typhoon events. The scatters are mainly concentrated in the range of -0.5 to 1 dB, where the reflectivity is less than 40 dBZ, that also indicates the stratiform precipitation. The closer Z_{DR} is to 0 dB, the smaller the precipitation particle is. The results indicate that the precipitation is mainly from the stratiform system, and the raindrop during three typhoon events is small-to-midsize particles. Many scatters are concentrated in the range of 0 to 2 dB, where $\log_{10} K_{DP}/10^{Z_H/10}$ is less than −4. The raindrop characteristics of the convective system during the three typhoon events are midsize particles.
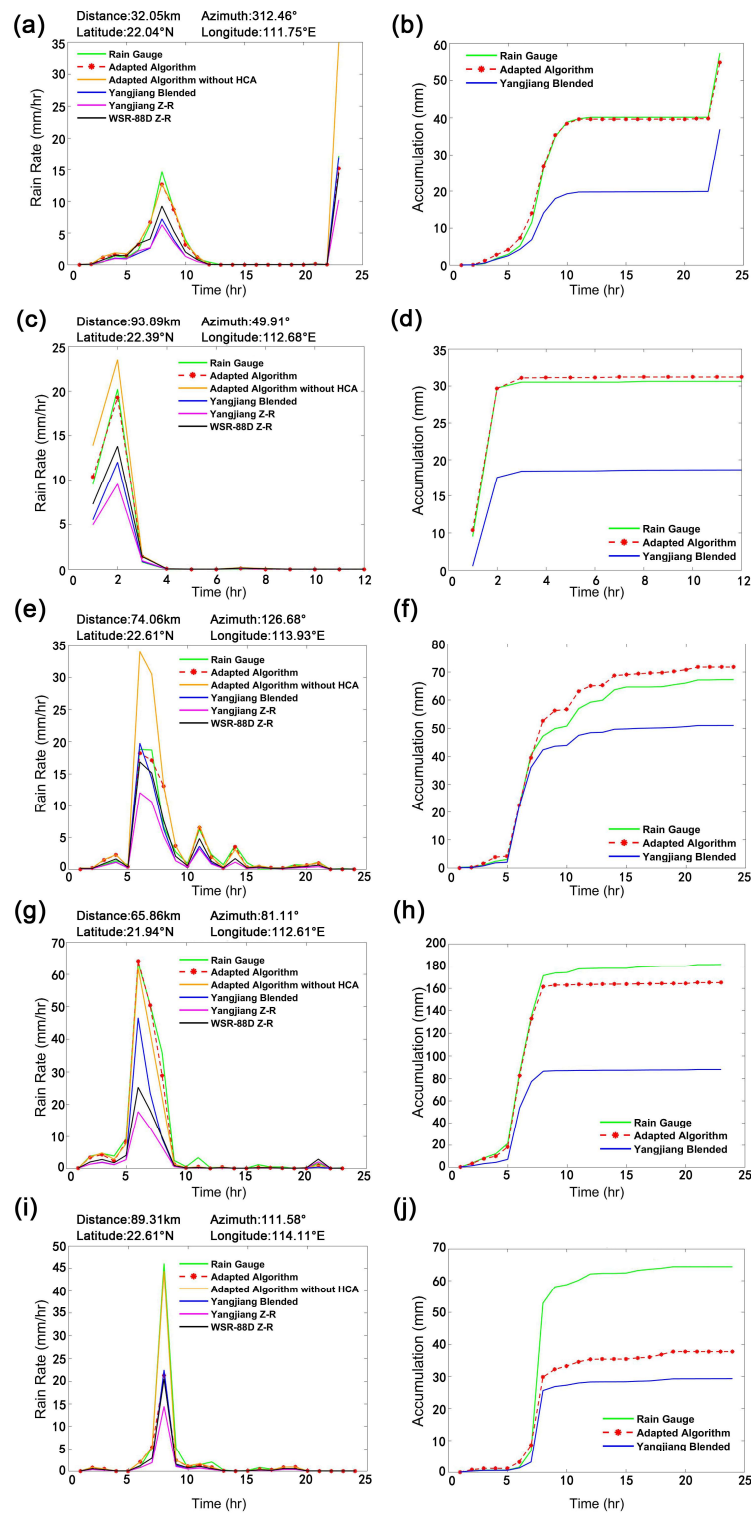
Figure 12. (**a**) Z_{DR} versus Z_H; (**b**) $\log_{10}[K_{DP}/(10^{Z_H/10})]$ versus Z_{DR}. The black dots are the simulated radar moments based on raindrop size distribution data.

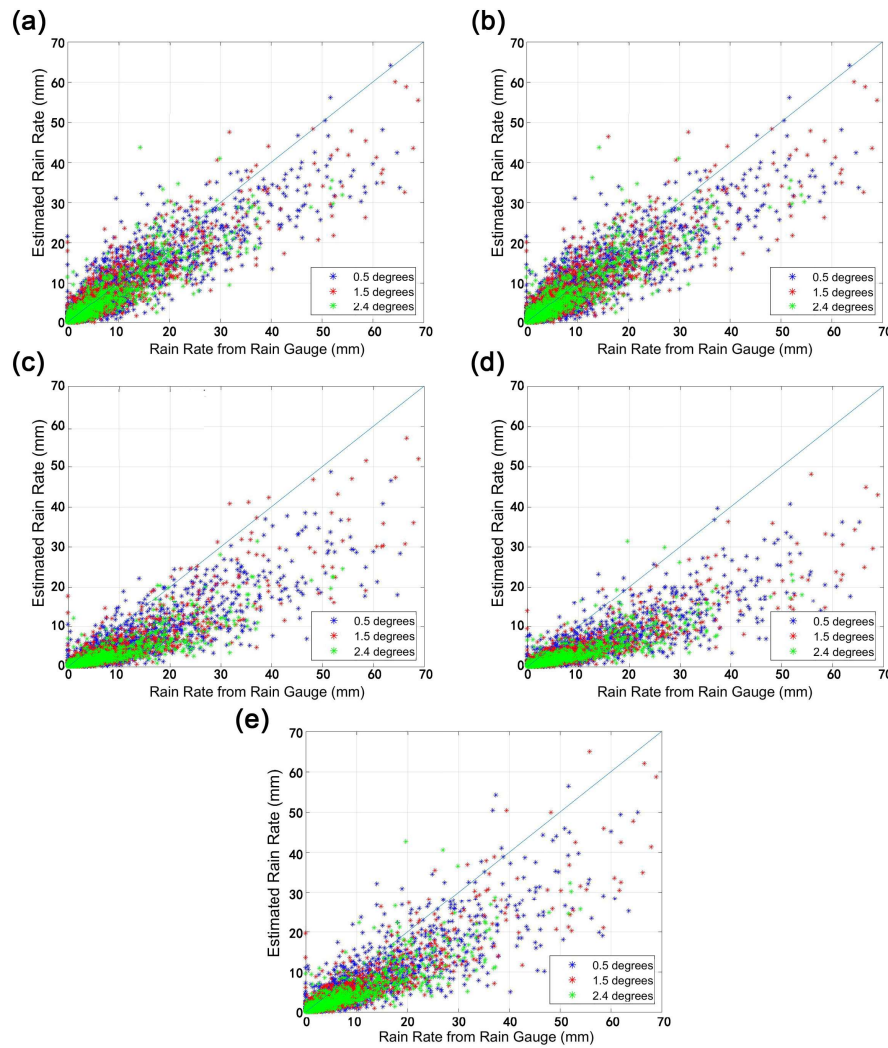## 4. QPE Results and Verification

4.1. Sample Results

The comparison of rain gauge measurements and the estimates from different radar rainfall algorithms for Typhoons Hato, Pakhar, and Mawar is shown in Figure 13. Among five rainfall algorithms, the adapted algorithm without HCA is applied to demonstrate HCA performance, which selects different rainfall relations based on the polarimetric parameters and hydrometeor classification results. For Hato and Pakhar, the data of 198 rain gauges within 100 km of the Yangjiang radar are used for comparison with the estimates computed by different algorithms, whereas the data of 809 rain gauges within 100 km of the Guangzhou radar are used for Mawar. As shown in Figure 13a, the estimates computed by the adapted algorithm agree well with the gauge measurements from 0700 to 0900 UTC, 23 August. The gauge, 712306, is located at a range of 32.05 km from the Yangjiang radar. Figure 13b shows the comparison of the accumulated rainfall corresponding to Figure 13a. Accumulation begins at 0000 UTC 23 August and the total gauge accumulation is 58.3 mm. The total accumulation of estimates from the adapted algorithm is 54.85 mm, whereas the total accumulation of estimates from the Yangjiang blended rainfall algorithm is 36.87 mm. For clarity, this paper mainly describes one of the gauges that is the best result, and other gauges (Figure 13c–j) are used to show various QPE results. The gauges illustrated in Figure 13c–j are chosen randomly, some of which show good agreement between radar estimates and gauge measurements, while others show relatively poor agreement. The adapted algorithm has better performance for QPE during typhoon events.

To further demonstrate the performance of different algorithms, the scatter plots of rain gauge measurements versus rainfall rates from various elevation angles are shown in Figure 14. The number of 2.4-degree scatter plots is less than 0.5-degree and 1.5-degree, which is related to data segmentation. The closer the scatters are to the 1:1 line, the better the estimation effect is. Figure 14a shows that most of the scatters (*CC* = 93.05%) for the QPE results of the adapted algorithm are distributed around the 1:1 line, whereas the QPE results of the Yangjiang blended rainfall algorithm, Yangjiang Z–R relation, and WSR-88D Z–R relation are usually below the 1:1 line. Although the results of the adapted algorithm without HCA are similar to those of the adapted algorithm, it is only slightly (*CC* = 0.55% not as good as the adapted algorithm due to the lack of HCA. In short, the adapted algorithm has better performance than other rainfall algorithms for QPE during typhoon events.

Figure 13. The rain gauge measurements (green line) and estimates computed by various radar algorithms at five selected gauge locations: (**a**), (**c**), (**e**), (**g**), (**i**) show the comparison of hourly rainfall rates; (**b**), (**d**), (**f**), (**h**), (**j**) show the comparison of accumulated rainfall. The rain gauge IDs are 712306, 716530, 713548, 716520, and 711166. The red dashed lines, yellow lines, blue lines, pink lines and black lines represent the rainfall estimates from the adapted algorithm, the adapted algorithm without HCA, Yangjiang blended rainfall algorithm, Yangjiang Z–R relation, and WSR-88D Z–R relation, respectively.

Figure 14. The scatter plots of radar rainfall estimates versus rain gauge measurements for all the events combined: (**a**) the adapted algorithm, (**b**) the adapted algorithm without HCA, (**c**) Yangjiang blended rainfall algorithm, (**d**) Yangjiang Z–R relation, and (**e**) WSR-88D Z–R relation.

4.2. Evaluation Metrics and Results

To quantify the performance of the adapted rainfall algorithm, a set of metrics is computed, including the normalized mean bias (*NMB*), normalized standard error (*NSE*), Pearson's correlation coefficients (*CC*), root-mean-square error (*RMSE*), and the Heidke skill score (*HSS*) [27–29], which are defined as follows:

$$NMB = \frac{\sum_{N=1}^{M}(R_N - G_N)}{\sum_{N=1}^{M} G_N},$$ (5a)

$$NSE = \frac{\sum_{N=1}^{M}|R_N - G_N|}{\sum_{N=1}^{M} G_N},$$ (5b)

$$CC = \frac{\sum_{N=1}^{M}(R_N - \overline{R_N})(G_N - \overline{G_N})}{\sqrt{\sum_{N=1}^{M}(R_N - \overline{R_N})^2 \sum_{N=1}^{M}(G_N - \overline{G_N})^2}},$$ (5c)

$$RMSE = \sqrt{\frac{\sum_{N=1}^{M}(R_N - G_N)^2}{M}},$$ (5d)

$$HSS = \frac{2(N_1 \times N_4 - N_2 \times N_3)}{(N_1 + N_3)(N_3 + N_4) + (N_2 + N_2)(N_2 + N_4)} \tag{5e}$$

where R_N and G_N represent the radar estimates and the rain gauge measurements at time frame N, respectively. M is the total sample number. The definitions of elements N_1, N_2, N_3, and N_4 are given in Table 2, and H is the hourly rainfall threshold. The value of *NMB* can be positive or negative. A positive value indicates overestimation, and a negative value stands for underestimation. *NSE* and *RMSE* are non-negative and *NSE* is not affected by rainfall. The closer *NMB*, *NSE*, and *RMSE* are to 0, the smaller the error is. *CC* indicates the correlation between the radar estimate and the "ground truth". The closer the value is to 1, the better the estimation effect is. Positive values of *HSS* indicate that the estimation is better, and a perfect estimation obtains a *HSS* of 1.

Table 2. Elements N_1, N_2, N_3, and N_4 are assigned the observed event counts in each category.

Radar	Rain Gauge	
	Observation $> H$ mm	**Observation $\leq H$ mm**
Estimate $> H$ mm	N_1	N_2
Estimate $\leq H$ mm	N_3	N_4

The results of *NMB*, *NSE*, *CC*, *RMSE*, and *HSS* of the five algorithms for Typhoons Hato, Pakhar, and Mawar are shown in Table 3. The *NSE*s of the adapted algorithm for the typhoon events are 38.38%, 30.4%, and 36.61%, respectively. The *RMSE* of the different algorithms for Hato are higher than for other typhoon events. The results show that the adapted algorithm has better performance for QPE than other algorithms, in terms of *NMB*, *NSE*, *CC*, *RMSE*, and *HSS*, but underestimates rainfall during the typhoon events. In general, the performance of the WSR-88D Z–R relation is better than that of the blended Yangjiang algorithm and Yangjiang Z–R relation for the three typhoon events combined, in terms of *NMB*, *NSE*, *CC*, and *HSS* ($H = 8$). The WSR-88D Z–R relation has lower *NSE* than the blended Yangjiang algorithm, but the blended Yangjiang algorithm has higher *CC* for three typhoon events than the WSR-88D Z–R relation. There is a large statistical difference between two algorithms in terms of *NMB*, *NSE*, *CC*, and *RMSE*, although the Yangjiang Z–R relation and WSR-88D Z–R relation are both Z–R rainfall relation. However, for the three typhoon events combined, the blended Yangjiang algorithm, WSR-88D Z–R relation, and Yangjiang Z–R relation significantly underestimate the rainfall rate.

The adapted algorithm has the same calculation processes as the "adapted algorithm without HCA", except for the inclusion of HCA. For the three typhoon events combined, the *RMSE*s of the two algorithms are 2.74 mm and 2.78 mm, respectively, and the *NSE*s of the two algorithms are 36.66% and 37.83%, respectively. The *HSS*s ($H = 0$) of the two algorithms are 68.52% and 34.05% for the three typhoon events combined, and the *HSS*s ($H = 8$) are 78.89% and 77.64%. The evaluation results from the adapted algorithm with and without HCA are similar, except the *HSS*s ($H = 0$). To investigate the reason, the polarimetric parameters and HCA results are analyzed. The adapted algorithm directly calculates rain rate using different rainfall relations, based on the hydrometeor classification results and polarimetric parameters, whereas other algorithms without HCA compute rainfall rate considering co-polar correlation coefficient ρ_{HV}. The reflectivity is very small or 0 where ρ_{HV} is less than 0.9. If ρ_{HV} is not considered, most of rain rates would be a constant, i.e., intercept of Z–R relation. Moreover, if the ice particles are partially melted, rain gauge would measure rainfall amount, but the radar estimated rainfall would be zero, as ρ_{HV} is less than 0.9 due to the ice contamination. Hence, using ρ_{HV} as the threshold is the main cause of the difference. In addition, the rainfall rate where "rain-hail mixture" is present, is ignored for the algorithms without HCA. As a result, the adapted algorithm has better performance for QPE than the adapted algorithm without HCA.

Table 3. Evaluation results of the various algorithms for Typhoons Hato, Pakhar, and Mawar. *NMB* is the normalized mean bias, *NSE* is normalized standard error, *CC* is the Pearson's correlation coefficient, *RMSE* is the root mean square error, and *HSS* is the Heidke skill score.

Event	Metrics	Algorithm				
		Adapted Algorithm	Adapted Algorithm without HCA	Blended Yangjiang Algorithm	Yangjiang Z–R Relation	WSR-88D Z–R Relation
Hato	*NMB* (%)	−15.46	−14.95	−47.97	−58.21	−39.00
	NSE (%)	38.38	39.54	52.51	61.16	48.68
	CC (%)	92.99	92.59	90.71	86.80	87.02
	RMSE (mm)	4.43	4.48	5.90	7.33	6.07
	HSS (%, *H* = 0)	63.13	36.58	36.74	36.70	36.42
	HSS (%, *H* = 8)	75.85	74.58	58.98	50.34	65.61
Pakhar	*NMB* (%)	−20.27	−20.47	−56.11	−64.22	−47.51
	NSE (%)	30.4	32.63	56.91	64.96	49.13
	CC (%)	94.76	93.37	91.39	93.82	94.08
	RMSE (mm)	2.55	2.79	4.42	5.01	3.90
	HSS (%, *H* = 0)	83.06	32.19	32.37	32.29	32.22
	HSS (%, *H* = 8)	89.14	87.62	55.30	34.26	69.30
Mawar	*NMB* (%)	−15.53	−15.97	−55.19	−58.84	−39.65
	NSE (%)	36.61	37.71	58.12	61.50	47.36
	CC (%)	92.92	92.36	91.05	91.13	91.72
	RMSE (mm)	2.37	2.40	3.47	3.75	2.88
	HSS (%, *H* = 0)	68.13	33.36	33.43	33.31	33.32
	HSS (%, *H* = 8)	78.42	77.18	51.48	46.95	63.39
All events	*NMB* (%)	−15.78	−16.00	−53.54	−58.99	−39.93
	NSE (%)	36.66	37.83	56.73	61.61	47.77
	CC (%)	93.05	92.50	91.02	89.74	90.24
	RMSE (mm)	2.74	2.78	3.95	4.49	3.56
	HSS (%, *H* = 0)	68.52	34.05	34.13	34.03	33.91
	HSS (%, *H* = 8)	78.89	77.64	53.73	47.00	64.55

Compared to the adapted algorithm without HCA, the Yangjiang blended rainfall algorithm has different rainfall relations. The *RMSE* of the adapted algorithm without HCA is 1.17 mm less than that of the Yangjiang blended rainfall algorithm for the three typhoon events combined. The QPE results indicate that different rainfall relations can make a big difference in the QPE performance for two algorithms. The specific rainfall relations of the adapted algorithm with and without HCA, and the Yangjiang blended rainfall algorithm are both derived from DSD data collected by a disdrometer in Yangjiang from April to July 2014, but the specific rainfall relations of the adapted algorithm with and without HCA are additionally adjusted for typhoon events. The specific rainfall relations of the adapted algorithm with and without HCA have better performance for QPE than the Yangjiang blended rainfall algorithm, due to their representation of the precipitation microphysical process. As the WSR-88D Z–R relation has been adjusted and demonstrated in the past, it better reflects the precipitation microphysical process than the Yangjiang Z–R relation. The WSR-88D Z–R relation shows better evaluation results than the Yangjiang Z–R relation for three typhoon events. The statistical difference between the WSR-88D Z–R relation and the Yangjiang Z–R relation further proves the conclusion about the effect of different rainfall relations. Due to various precipitation types in the typhoon system, different rainfall equations, i.e., $R(Z_H)$, $R(K_{DP})$, $R(Z_H, Z_{DR})$, and $R(Z_{DR}, K_{DP})$, should be mixed and applied for typhoon events. The blended Yangjiang algorithm has additional rainfall relations compared to the Yangjiang Z–R relation, and the QPE performance of the Yangjiang algorithm is better than the Yangjiang Z–R relation.

5. Conclusions

Typhoons are often accompanied by strong convective weather such as high winds and heavy rainfall, resulting in catastrophic flash floods. Accurate QPE is one of the essential requirements for

hazard mitigation and disaster management during typhoon events. In this paper, an adapted radar rainfall system combining data QC and segmentation, HCA, and quantitative rainfall estimation is detailed and applied for three typhoon events in southern China. Dual-polarization radar observations from the Yangjiang and Guangzhou radars are examined to demonstrate the performance of the rainfall estimation algorithm. These radars are among the first batch of the dual-polarization upgrade of the operational weather radar network in China. Therefore, the results of this study will facilitate the operational use of polarimetric measurements in QPE applications in China.

In addition, precipitation microphysical analyses are examined, along with the detailed QPE analysis. The size and concentration of raindrops in convective precipitation during Typhoon Hato in this study are consistent with the results in Bringi et al. [25] for "maritime-like" precipitation clusters and Wen et al. [26] for landing typhoons in China. The convective and stratiform precipitation of Typhoon Mawar shows a smaller size and a higher concentration of raindrops than that of Typhoon Hato. Assuming rainfall measurements from the ground rain gauges are the "truth", the rainfall estimates computed by different algorithms are evaluated. The results show that the QPE performance of the adapted algorithm is better than other algorithms for all the three typhoon events, in terms of *NMB*, *NSE*, *CC*, *RMSE*, and *HSS*. The evaluation results from the adapted algorithm with and without HCA are similar, except the *HSS*s ($H = 0$). Although HCA combining different polarimetric observables can slightly improve the QPE performance, HCA is inadequate to quantify the rainfall rate where "rain-hail mixture" is present. In addition, different rainfall relations offer various QPE performance for typhoon events due to their representation of the precipitation microphysical process. Blending of different rainfall equations, i.e., $R(Z_H)$, $R(K_{DP})$, $R(Z_H, Z_{DR})$, and $R(Z_{DR}, K_{DP})$ shows better performance for QPE than a single rainfall equation. In conclusion, this work provides a comprehensive radar rainfall analysis of representing typhoon events. It is expected that the local meteorological bureaus can implement the improved radar rainfall algorithms to enhance rainfall mapping, which in turn would help to mitigate losses from hazardous weather phenomena. Future work will focus on microphysical retrievals using polarimetric radar measurements during typhoon events.

Author Contributions: Q.X. and W.Z. carried out the detailed analysis. H.C. supervised this study. Q.X. and H.C. prepared the first draft of this manuscript. W.-c.L. and L.H. reviewed and edited the manuscript. Q.X., H.C., W.-c.L., W.Z., Y.M. discussed the analysis results. X.L. provided the disdrometer data. All authors have read and agreed to the published version of the manuscript.

Conflicts of Interest: The authors declare no conflicts of interest.

References

1. Wolff, D.B.; Petersen, W.A.; Tokay, A.; Marks, D.A.; Pippitt, J.L. Assessing Dual-Polarization Radar Estimates of Extreme Rainfall during Hurricane Harvey. *J. Atmos. Oceanic Technol.* **2019**, *36*, 2501–2520. [CrossRef]
2. Baeck, M.L.; Smith, J.A. Rainfall Estimation by the WSR-88D for Heavy Rainfall Events. *Wea. Forecast.* **2010**, *13*, 416–436. [CrossRef]
3. Bringi, V.N.; Chandrasekar, V. *Polarimetric Doppler Weather Radar: Principles and Applications*; Cambridge University Press: Cambridge, UK, 2001; p. 648.
4. Seliga, T.A.; Bringi, V.N. Potential use of radar differential reflectivity measurements at orthogonal polarizations for measuring precipitation. *J. Appl. Meteor.* **1976**, *15*, 69–76. [CrossRef]
5. Wen, G.; Chen, H.; Zhang, G.; Sun, J. An inverse model for raindrop size distribution retrieval with polarimetric variables. *Remote Sens.* **2018**, *10*, 1179. [CrossRef]

6.	Ryzhkov, A.V.; Schuur, T.J.; Burgess, D.W.; Heinselman, P.L.; Giangrande, S.E.; Zrnić, D.S. The joint polarization experiment: Polarimetric rainfall measurements and hydrometeor classification. *Bull. Amer. Meteor. Soc.* **2005**, *86*, 809–824. [CrossRef]

7.	Ryzhkov, A.; Diederich, M.; Zhang, P.; Simmer, C. Potential Utilization of Specific Attenuation for Rainfall Estimation, Mitigation of Partial Beam Blockage, and Radar Networking. *J. Atmos. Oceanic Technol.* **2014**, *31*, 599–619. [CrossRef]

8.	Chandrasekar, V.; Bringi, V.N.; Balakrishnan, N.; Zrnić, D.S. Error structure of multiparameter radar and surface measurements of rainfall. *J. Atmos. Ocean. Technol.* **1988**, *5*, 783–795. [CrossRef]

9.	Gorgucci, E.; Scarchilli, G.; Chandrasekar, V. A robust estimator of rainfall rate using differential reflectivity. *J. Atomos. Ocean. Technol.* **1994**, *11*, 586–592. [CrossRef]

10.	Chen, H.; Chandrasekar, V. The quantitative precipitation estimation system for Dallas–Fort Worth (DFW) urban remote sensing network. *J. Hydrol.* **2015**, *531*, 259–271. [CrossRef]

11.	Gou, Y.; Ma, Y.; Chen, H.; Yin, J. Utilization of a C-band polarimetric radar for severe rainfall event analysis in complex terrain over Eastern China. *Remote Sens.* **2019**, *11*, 22. [CrossRef]

12.	Cifelli, R.; Chandrasekar, V.; Lim, S.; Kennedy, P.C.; Wang, Y.; Rutledge, S.A. A new dual-polarization radar rainfall algorithm: Application in Colorado precipitation events. *J. Atmos. Ocean. Technol.* **2011**, *28*, 352–364. [CrossRef]

13.	Huang, H.; Zhao, K.; Chen, H.; Hu, D.; Fu, P.; Lin, Q.; Yang, Z. Improved Attenuation-based Radar Precipitation Estimation Considering the Azimuthal Variabilities of Microphysical Properties. *J. Hydrometeor.* **2020**, (in press).

14.	Bechini, R.; Chandrasekar, V. A semisupervised robust hydrometeor classification method for dual-polarization radar applications. *J. Atmos. Oceanic Technol.* **2015**, *32*, 22–47. [CrossRef]

15.	Yu, Z.; Wang, Y.; Xu, H.; Davidson, N.; Chen, Y.; Chen, Y.; Yu, H. On the relationship between intensity and rainfall distribution in tropical cyclones making landfall over China. *J. Appl. Meteor. Climatol.* **2017**, *56*, 2883–2901. [CrossRef]

16.	Wang, Y.; Chandrasekar, V. Algorithm for Estimation of the Specific Differential Phase. *J. Atmos. Ocean. Technol.* **2009**, *26*, 2565–2578. [CrossRef]

17.	Chen, H.; Chandrasekar, V. An improved dual-polarization radar rainfall algorithm (DROPS2.0): Application in NASA IFloods field campaign. *J. Hydrometeor.* **2017**, *18*, 917–937. [CrossRef]

18.	Chen, H.; Lim, S.; Chandrasekar, V.; Jang, B.J. Urban hydrological applications of dual-polarization x-band radar: Case study in korea. *J. Hydrol. Eng.* **2016**, *22*(5), E5016001.1–E5016001.13. [CrossRef]

19.	Gou, Y.; Chen, H.; Zheng, J. An improved self-consistent approach to attenuation correction for C-band polarimetric radar measurements and its impact on quantitative precipitation estimation. *Atmos. Res.* **2019**, *226*, 32–48. [CrossRef]

20.	Waterman, P.C. Matrix formulation of electromagnetic scattering. *Proc. IEEE.* **1965**, *53*, 805–812. [CrossRef]

21.	Thurai, M.; Huang, G.J.; Bringi, V.N.; Randeu, W.L.; Schoenhuber, M. Drop shapes, model comparisons, and calculations of polarimetric radar parameters in rain. *J. Atmos. Ocean. Technol.* **2007**, *24*, 1019–1032. [CrossRef]

22.	Maddox, R.A.; Zhang, J.; Gourley, J.J.; Howard, K.W. Weather radar coverage over the contiguous United States. *Wea. Forecast.* **2002**, *17*, 927–934. [CrossRef]

23.	Matrosov, S.Y.; Ralph, F.M.; Neiman, P.J.; White, A.B. Quantitative assessment of operational weather radar rainfall estimates over California's Northern Sonoma County using HMT-West data. *J. Hydrometeorol.* **2014**, *15*, 393–410. [CrossRef]

24.	Fulton, R.A.; Breidenbach, J.P.; Seo, D.J.; Miller, D.A.; O'Bannon, T. The WSR-88D Rainfall Algorithm. *Wea. Forecast.* **1998**, *13*, 377–395. [CrossRef]

25.	Bringi, V.N.; Chandrasekar, V.; Hubbert, J.; Gorgucci, E.; Randeu, W.L.; Schoenhuber, M. Raindrop size distribution in different climatic regimes from disdrometer and dual-polarized radar analysis. *J. Atmos. Sci.* **2003**, *60*, 354–365. [CrossRef]

26.	Wen, L.; Zhao, K.; Chen, G.; Wang, M.; Zhou, B.; Huang, H.; Hu, D.; Lee, W.C.; Hu, H. Drop size distribution characteristics of seven typhoons in China. *J. Geophys. Res. Atmos.* **2018**, *123*, 6529–6548. [CrossRef]

27.	Barnston, A.G. Correspondence among the correlation, RMSE, and Heidke forecast verification measures: Refinement of the Heidke score. *Wea. Forecast.* **1992**, *7*, 699–709. [CrossRef]

28. Conner, M.D.; Petty, G.W. Validation and intercomparison of SSM/I rain-rate retrieval methods over the continental Unites States. *J. Appl. Meteor.* **1998**, *37*, 679–700. [CrossRef]

29. Anagnostou, M.N.; Kalogiros, J.; Marzano, F.S.; Anagnostou, E.N.; Montopoli, M.; Piccioti, E. Performance evaluation of a new dual-polarization microphysical algorithm based on long-term x-band radar and disdrometer observations. *J. Hydrometeorol.* **2013**, *14*, 560–576. [CrossRef]